ACS APPLIED MATERIALS & INTERFACES

Research Article

Cite This: ACS Appl. Mater. Interfaces 2019, 11, 38633−38640

www.acsami.org

Two-Dimensional Cobalt Phosphate Hydroxide Nanosheets: A New Type of High-Performance Electrocatalysts with Intrinsic CoO_6 Lattice Distortion for Water Oxidation

Xiuming Bu,[▲,†,‡] ChaoLung Chiang,[▲,§] Renjie Wei,[‡] Zebiao Li,[‡] You Meng,[‡] ChunKuo Peng,[§,∥] YuChang Lin,[§,∥] Yangyang Li,[‡] YanGu Lin,[*,§] Kwok Sum Chan,[†,¶] and Johnny C. Ho[*,‡,¶,⊥]

[†]Department of Physics, [‡]Department of Materials Science and Engineering and [¶]Centre of Functional Photonics, City University of Hong Kong, Kowloon, Hong Kong SAR, P.R. China

[§]National Synchrotron Radiation Research Center, Hsinchu 30076, Taiwan, ROC

[∥]Department of Materials Science and Engineering, National Chiao Tung University, Hsinchu 30010, Taiwan, ROC

[⊥]Shenzhen Research Institute, City University of Hong Kong, Shenzhen 518057, P.R. China

Supporting Information

ABSTRACT: Despite the recent advances in electrochemical water splitting, developing cost-effective and highly efficient electrocatalysts for oxygen evolution reaction (OER) still remains a substantial challenge. Herein, two-dimensional cobalt phosphate hydroxides ($Co_5(PO_4)_2(OH)_4$) nanosheets, a unique stacking-disordered phosphate-based inorganic material, are successfully prepared via a facile and scalable method for the first time to serve as a superior and robust electrocatalyst for water oxidation. On the basis of the detailed characterization (e.g., X-ray absorption near-edge structure and X-ray photoelectron spectroscopy), the obtained nanosheets consist of special zigzag CoO_6 octahedral chains along with intrinsic lattice distortion and excellent hydrophilicity, in which these factors contribute to the highly efficient performance of prepared electrocatalysts for OER. Specifically, $Co_5(PO_4)_2(OH)_4$ deposited on glassy carbon electrode (loading amount ≈0.553 mg cm^{-2}) can exhibit an unprecedented overpotential of 254 mV to drive a current density of 10 mA cm^{-2} with a small Tafel slope of 57 mV dec^{-1} in alkaline electrolytes, which outperforms the ones of $Co_3(PO_4)_2$ (370 mV) and $Co(OH)_2$ (360 mV) as well as other advanced catalysts. Evidently, this work has opened a new pathway to the rational design of promising metal phosphate hydroxides toward the efficient electrochemical energy conversion.

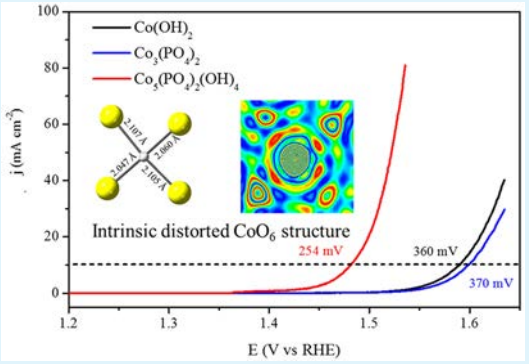

KEYWORDS: *$Co_5(PO_4)_2(OH)_4$, nanosheet, lattice distortion, electrocatalyst, oxygen evolution reaction*

INTRODUCTION

In recent years, the problems of continuous fossil fuel consumption and uncontrolled greenhouse gas emission have driven intensive research on innovative technologies to generate clean energies through sustainable electrocatalytic water splitting.[1] In water splitting, hydrogen and oxygen gases are typically generated via two half reactions, namely, hydrogen evolution reaction (HER) and oxygen evolution reaction (OER). As compared to those of HER, the high overpotential and the sluggish reaction kinetics of OER ($4OH^- \rightarrow 2H_2O + O_2 + 4e^-$) have heavily restricted the efficiency of overall water splitting. Until now, precious-noble-metal oxides (e.g., IrO_2 and RuO_2) are usually used as the state-of-the-art electrocatalysts for OER. However, the high cost and poor long-term stability of these noble materials inevitably limit their industrial utilizations. In this regard, substantial works are currently focused on the development of highly efficient and non-precious-metal-based electrocatalysts, including transition-metal oxides,[2−4] transition-metal hydroxides,[5−7] transition-metal chalcogenides/carbides,[8,9] transition-metal borides/nitrides,[10,11] and carbon-based materials.[12,13]

Among many promising material candidates, phosphate-based materials play an indispensable role there. Back in 2008, Nocera and co-workers reported the first cobalt phosphate (CoPi) as being an excellent electrocatalyst for water oxidation in neutral pH condition.[14] After that, many phosphate-based materials were then explored, such as NiPi,[15,16] FePi,[17] IrPi,[18] etc. Lately, Driess et al. developed a new kind of phosphate as a bifunctional catalyst, $Ni_{11}(HPO_3)_8(OH)_6$, that can reach a water-splitting current density of 10 mA cm^{-2} simply by applying a cell voltage of 1.6 V.[19] In addition to developing new materials, some research groups have also adopted several

Received: July 6, 2019
Accepted: September 24, 2019
Published: September 24, 2019

DOI: 10.1021/acsami.9b11594
ACS Appl. Mater. Interfaces 2019, 11, 38633−38640

approaches to further improve their electrocatalytic activity, which involves electronic structure and morphology modification as well as coupling with highly conductive materials. For instance, Xu's group demonstrated the cobalt phosphate nanoparticles decorated with nitrogen-doped carbon layers using a hydrothermal method, where this hybrid material system can exhibit excellent catalytic performance in 1 M KOH electrolyte.[20] Also, Zhang's group prepared $Co_3(PO_4)_2$–Co_3O_4 mesoporous nanosheet hybrid networks that can yield high performance and excellent stability in alkaline electrolyte.[21] Evidently, these examples suggest the potential of further enhancing metal-phosphates-based materials as high-performance electrocatalysts.

This work, to the best of our knowledge, is the first report to investigate a novel, efficient, and robust cobalt phosphate hydroxide ($Co_5(PO_4)_2(OH)_4$) prepared via a simple hydrothermal method for alkaline electrochemical OER. Importantly, the $Co_5(PO_4)_2(OH)_4$ catalyst exhibits a much lower overpotential of only 254 mV at a current density of 10 mA cm^{-2} on the glassy carbon electrode with a mass loading of 0.553 mg cm^{-2} and a small Tafel slope of 57 mV dec^{-1}. On the basis of thorough structural analysis (e.g., X-ray absorption near-edge structure (XANES) and X-ray photoelectron spectroscopy (XPS)), excellent electrocatalytic performance of $Co_5(PO_4)_2(OH)_4$ resulted from its abundant electrochemical active sites exposed in the constituent zigzag edges of CoO_6 octahedron, easier formation of active species in the distorted CoO_6 structure, and its outstanding hydrophilic characteristics. All these results can clearly confirm the metal phosphate hydroxides as a new type of stable electrocatalysts for highly efficient oxygen evolution reaction.

EXPERIMENTAL SECTION

Preparation of Cobalt Phosphate Hydroxide, Cobalt Phosphate, and Cobalt Hydroxide. *Synthesis of Cobalt Phosphate Hydroxide.* Typically, two solutions were first prepared by dissolving 0.3 g of $Co(NO_3)_2{\cdot}6H_2O$ in 5 mL of deionzed water and 0.08 g of $(NH_4)H_2PO_4$ in 5 mL of deionzed water, respectively. After the solutions were stirred for 5 min, the $(NH_4)H_2PO_4$ solution was slowly added into the $Co(NO_3)_2{\cdot}6H_2O$ solution. Next, the pH of the processed solution was slowly adjusted to the value of 12 via the addition of NH_4OH solution. The mixture was then transferred into a 15 mL Teflon-lined stainless-steel autoclave and heated for 180 °C for 48 h. Fianlly, the product was obtained by centrifugation, washed thoroughly with deionized water and ethanol three times each, and dried at 60 °C.

Synthesis of Cobalt Phosphate. Cobalt phosphate was prepared according to a previous report.[20] In detail, 0.3 g of $Co(NO_3)_2{\cdot}6H_2O$ and 0.12 g of Na_3PO_4 were added into 10 mL of deionzed water. After the mixture was stirred for 10 min, it was transferred into a 15 mL Teflon-lined stainless-steel autoclave and heated for 120 °C for 6 h. The product was then washed with deionized water and ethanol three times each, collected by centrifugation, and dried at 60 °C.

Synthesis of Cobalt Hydroxide. Specifically, 1.2 g of $Co(NO_3)_2{\cdot}6H_2O$ and 0.02 g of $C_6H_{12}N_4$ were added into 40 mL of deionized water. After the mixture was stirred for 10 min, it was transferred into a 15 mL Teflon-lined stainless-steel autoclave and heated for 180 °C for 6 h. The product was then washed with deionized water and ethanol three times each, collected by centrifugation, and dried at 60 °C.

Characterization. Scanning electron microscopy (SEM, Phenom Pro, Phenom-World, The Netherlands) conducted at 10 kV was utilized to observe the morphologies and the dimensions of fabricated samples. The valence state and the surface composition were assessed via X-ray photoelectron spectroscopy (XPS) with a VG Multilab 2000 system using a photoelectron spectrometer (Thermo Fisher Scientific, Waltham, MA, USA). All XPS peak positions were calibrated with the carbon peak position. Their crystal structural information was obtained using a Bruker D2 Phaser (Bruker, Billerica, MA, USA) with Cu Kα radiation (λ = 0.15406 nm). The corresponding Fourier-transform infrared spectroscopy (FT-IR) spectra were recorded from KBr disks using a PerkinElmer GX instrument in the wavenumber range of 4000−500 cm^{-1}. Contact angle measurements were carried out on a standard testing machine integrated with a CCD camera. Electron density mapping was obtained from software Crystal Maker X.

Electrochemical Measurements. Gamry G300 potentiostat was employed to operate all electrochemical measurements at room temperature. A typical process for preparing the electrode is depicted as follows. The fabricated electrocatalyst (5 mg) and Nafion (20 μL, 5 wt %) were dispersed in a deionized water/ethanol (volume ratio, 5:17) mixture solution (440 μL) by ultrasonication to obtain a homogeneous ink. Then the electrocatalyst ink (10 μL) was dropped onto a polished glassy carbon electrode (0.19625 cm^2) with a diameter of 5 mm (loading amount ≈0.553 mg cm^{-2}). After overnight drying (8 h), the fabricated electrode can serve as the working electrode. For catalysts fabricated on the nickel foam, the electrochemical activity and stability tests were carried in 1 M KOH (pH 13.71) with a three-electrode configuration where the processed glassy carbon electrode, carbon rod, and saturated calomel electrode (SCE, Ag/AgCl) were used as the working electrode, counter electrode, and reference electrode, respectively. Linear sweep voltammetry (LSV) polarization curves were recorded to investigate the OER performance in 1 M KOH electrolyte (pH 13.71) at a scan rate of 5 mV s^{-1}. Unless otherwise mentioned, all the electrochemical data collected were *iR*-corrected automatically. According to the Nernst equation, $E_{RHE} = E_{exp} + E_{SCE} + 0.059 \times pH$, all potentials expressed here are converted to reversible hydrogen electrode (E_{RHE}), where E_{exp} is the recorded potential against Ag/AgCl reference electrode. Electrochemical impedance spectroscopy (EIS) conducted from 0.01 Hz to 300 kHz was used to determine the charge-transfer resistance. The total amount of produced gas (H_2 and O_2) was conducted via gas chromatography (GC-2014, Shimadzu). The Faraday efficiency (FE) was calculated based on the equation of nF/It, where n is the number of electrons needed for product (2 for H_2 and 4 for O_2, respectively), I is the recorded current (A), t is the reaction time (s), and F is the Faraday constant (96 485.338 C mol^{-1}).

X-ray Absorption Spectroscopy (XAS) Measurement. X-ray absorption near-edge structure (XANES) and its derivative spectra were collected at Taiwan Photon Source beamline (TPS 44A) station of National Synchrotron Radiation Research Center (NSRRC) in Hsinchu, Taiwan, to identify the valences of cobalt (Co) in the sample powder. The TPS 44A station located within the electron storage ring was operated at an energy of 3.0 GeV and a ring current of 500 mA. A Lytle detector in the energy range of Co K edge (7709 eV) was adopted for the XANES spectra collection at room temperature. For data processing, the collected XANES spectra were first calibrated with a signal of the cobalt foil and then normalized using Athena software (version 0.9.26). Extended X-ray absorption fine structure (EXAFS) spectra were converted to the wavevector *K*- and *R*-space forms for the comparison of each other to identify the average local environment of the sample around the target Co atoms for further discussions.

RESULTS AND DISCUSSION

Here, the cobalt phosphate hydroxides, $Co_5(PO_4)_4OH_2$ (CPH), are prepared via a simple hydrothermal method. For a fair comparison, $Co_3(PO_4)_2$ (CP) and $Co(OH)_2$ (CH) are also constructed to compare their OER performances against CPH. To begin with, we employed XRD to investigate the chemical composition and the structure of obtained products. As illustrated in the XRD patterns of CP, CH, and CPH in the Supporting Information (Figure S1), there are multiple

DOI: 10.1021/acsami.9b11594
ACS Appl. Mater. Interfaces 2019, 11, 38633−38640

characteristic peaks observed, which are associated with the orthorhombic cobalt phosphate hydroxide $Co_5(PO_4)_2(OH)_4$ (JCPDS no. 70-0515). The photograph image (Supporting Information, Figure S2) also shows that these three samples yield different colors in the appearance. Both CP and CPH give the purplish color, while CH exhibits the pink color, indicating the difference in their electronic structures. At the same time, Fourier transform infrared spectroscopy (FTIR) is also employed to disclose the chemical composition and bonding state of all the samples (Supporting Information, Figure S3). Evidently, there are three major peaks located at 1040, 1090, and 1618 cm^{-1}, which are attributed to the P−O stretching bonds.[22] Other dominant peaks appearing in the range of 2750−3600 cm^{-1} can be assigned to the O−H stretching vibration associated with the water and exchangeable OH^-.[19] It is also noted that there is a minor peak observed at 1350 cm^{-1} for both CH and CPH, this peak being absent in CP, further verifying the presence of OH moiety in CPH. All these findings can undoubtedly confirm the composition and structure of fabricated compounds.

In addition, the morphologies of these samples are also thoroughly investigated by scanning electron microscopy (SEM) and transmission electron microscopy (TEM). As depicted in the SEM image of obtained CP and CH samples in the Supporting Information (Figure S4a,b), CP gives a layered structure while CH exhibits a nanowire morphology. The diameter of this nanowire is found to be around 240 nm. Interestingly, the CPH sample yields a nanosheet configuration (Figure 1a,b) that is similar to the one witnessed for CP. On

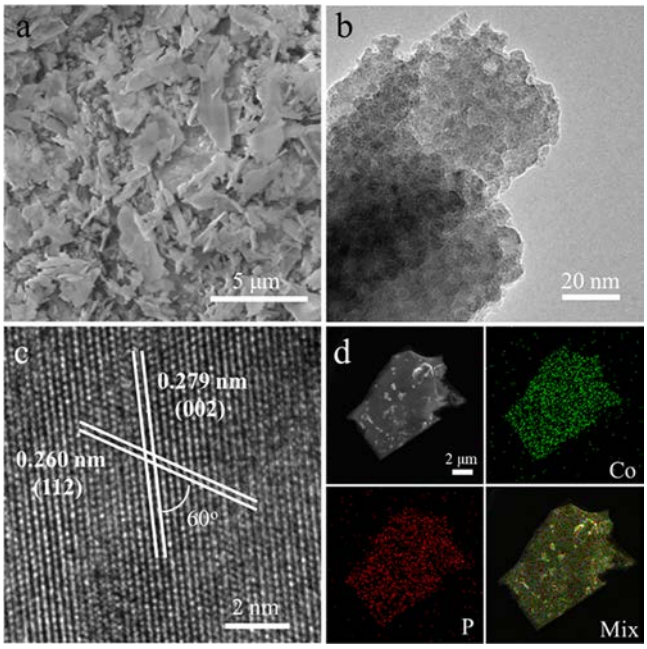

Figure 1. (a) SEM image, (b) TEM image, and (c) HRTEM image of CPH; (d) EDX mapping of different elemental constituents of the CPH sample.

the basis of the detailed SEM analysis, the average layer thickness of CP is determined to be 287.5 nm, which is obviously larger than the value (55.8 nm) of CPH (Supporting Information, Figure S5). This reduced layer thickness indicates that the CPH sample possesses the larger surface area there. However, the surface area of two-dimensional (2D) nanosheets is typically smaller than that of nanowires. In this case, the specific surface area (SSA) of these samples is anticipated to come after the following trend: $SSA_{CP} < SSA_{CPH} < SSA_{CH}$. Indeed, the Brunauer−Emmett−Teller (BET) measurement results further confirm this trend, where the CH sample has the largest SSA of 30.410 $m^2\ g^{-1}$, followed by CPH (11.642 $m^2\ g^{-1}$) and CH (8.543 $m^2\ g^{-1}$), accordingly (Supporting Information, Figure S6). Also, an HRTEM image of the product is shown in Figure 1c. The clear lattice fringes of ca. 0.279 and 0.260 nm correspond to the (002) and (112) planes, respectively. More importantly, as presented in the elemental mapping of CPH nanosheets in Figure 1d, the distribution of all constituents (i.e., Co, P, and O) are highly uniform, indicating the homogeneous composition of obtained samples via our simple synthesis method. This nanosheet morphology with enhanced surface area as well as uniform composition of the CPH sample would be essential for further development as a highly efficient electrocatalyst.

Apart from the composition and morphology, the electrocatalytic OER performance of CP, CH, and CPH are also evaluated in detail as these catalyst samples are deposited onto the glassy carbon electrode operating in a typical three-electrode system in 1 M KOH. In comparison, commerical RuO_2 was chosen as the reference. Particularly, Figure 2a depicts the OER linear sweep voltammetry (LSV) polarization curves of the glassy carbon electrodes loaded with different catalyst samples. The mass loading of the catalyst is kept as 0.553 mg cm^{-2} for each sample tested. It is clear that both CP and CH exhibit relatively large overpotentials of 370 and 360 mV, respectively, at a current density of 10 mA cm^{-2}. In contrast, the CPH catalyst and RuO_2 are highly active for OER, which can reach the same current density of 10 mA cm^{-2} with only an overpotential of 254 and 256 mV. Tafel plots were obtained from the LSV curves, indicating the kinetic properties of OER progress as shown in Figure 2b. The excellent electrocatalytic performance of CPH can be proved by its small Tafel slope of 57 mV dec^{-1}, which is smaller than those of CH (210 mV dec^{-1}) and CP (246 mV dec^{-1}) in the range of high overpotential, accordingly. Co-based materials have been studied for OER for a long time and the common consensus for the electrocatalysis of OER is a heterogeneous reaction in which the bonding interactions within the intermediates (M−OH, M−O, and M−OOH) followed by O−O formation as shown below:[23]

$$M{-}OH_2 + OH^- \rightarrow M{-}OH + H_2O + e^- \quad (1)$$

$$M{-}OH + OH^- \rightarrow M{-}O^* + H_2O + e^- \quad (2)$$

$$M{-}O^* + OH^- \rightarrow M{-}OOH + e^- \quad (3)$$

$$M{-}OOH + OH^- \rightarrow M{-}OH_2 + O_2 + e^- \quad (4)$$

In this case, the relatively large Tafel slopes of CH and CP prove that the rate-limiting step of OER processes is located in the first step described above where one electron is transferred, which is consistent with previous reports.[24,25] At the same time, the Tafel slopes of CPH and RuO_2 are close to the featured Tafel slope of 60 mV dec^{-1}, indicating a different rate-limiting step here. These superior OER characteristics of CPH are even comparable to other state-of-the-art electrocatalysts, such as Ni_3N−NiMoN/CF,[26] NiMo/Ti mesh,[27] and CoFe-PO/NF[28] (Supporting Information, Table S1).

In general, electrochemical active surface areas (ECSA) play an important role in electrocatalytic reactions. In this work, the

DOI: 10.1021/acsami.9b11594
ACS Appl. Mater. Interfaces 2019, 11, 38633−38640

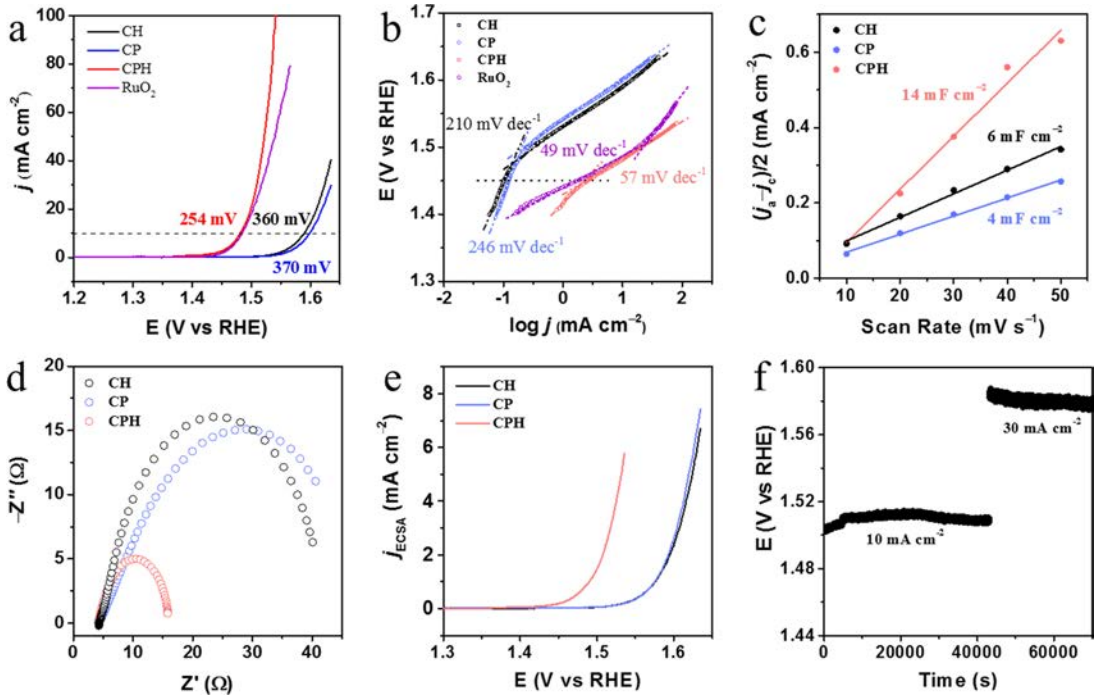

Figure 2. (a) OER polarization curve of CP, CH, and CPH deposited onto glassy carbon electrodes. The sweep rate is 5 mV s^{-1} in 1 M KOH. (b) Corresponding Tafel slope plots. (c) ECSA evaluation from the plots of the current density at 0.15 V vs RHE. (d) EIS spectra of all samples at an overpotential of 350 mV. (e) Specific current densities of all samples obtained via normalizing the geometric current densities to the ECSA. (f) Stability test of CPH at the current density of 10 mA cm^{-2} and then 30 mA cm^{-2}.

Table 1. Summary of the BET and Electrochemical Properties of Different Catalyst Samples

catalyst	BET (m^2 g^{-1})	C_{dl} (μF cm^{-2})	C_{dl}/BET	j (mA cm^{-2})	overpotential (mV)	Tafel slope (mV dec^{-1})
CP	8.543	4	0.468	10	370	246
CH	30.410	6	0.197	10	360	210
CPH	11.264	14	1.243	10	254	57

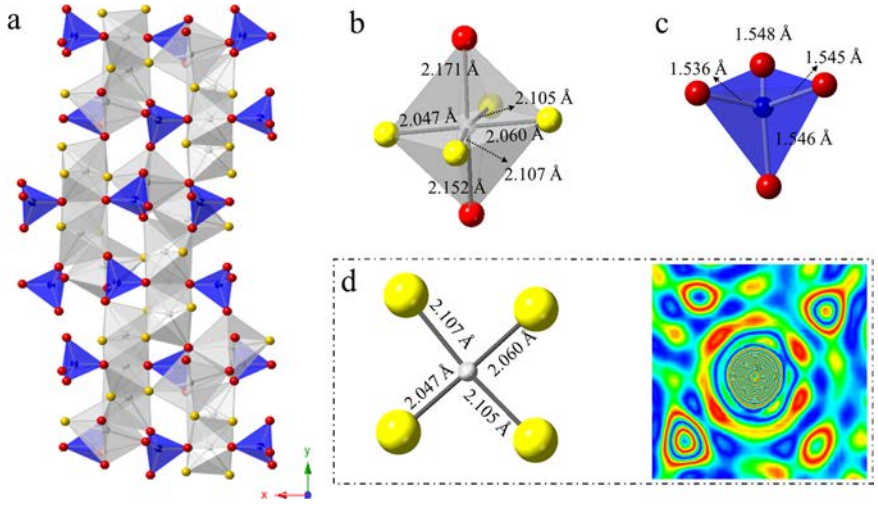

Figure 3. (a) Schematic diagrams illustrating the crystal structure of $Co_5(PO_4)_2(OH)_4$ with different orientations, which comprises the constituent zigzag double chains connected by $(PO_4)^{3-}$ groups. (Co, gray; P, blue; O, red; O−H, yellow). (b) Cell structure of CoO_6 octahedron and (c) phosphate tetrahedron after distortion. Inset number is the bond length after distortion commonly reported in the literature. (d) Cross section of the (001) plane in the CoO_6 octahedron and corresponding electron density mapping.

ECSA of all samples are carefully evaluated via cycle voltammetry at different scan rates as shown in the Supporting Information (Figure S7). It is obvious that CPH possesses double layer capacitance (C_{dl}) of 14 mF cm^{-2} that is nearly 3.5 times and 2.3 times larger than those of CP (4 mF cm^{-2}) and CH (6 mF cm^{-2}), which proves that CPH exposes more electrochemical active sites and surface areas than CP and CH samples.[29] The electrochemical impedance spectroscopy (EIS) plots also reveal the ionic and ohmic resistance of CPH being much smaller than those of CP and CH, indicating that CPH

DOI: 10.1021/acsami.9b11594
ACS Appl. Mater. Interfaces 2019, 11, 38633−38640

has better electrical conductivity (Figure 2d), which is in good agreement with the above-discussed Tafel analysis.[30] Meanwhile, the same consistent phenomenon can be observed in the OER performance assessment without *iR* compensation. As given in the Supporting Information (Figure S8), CPH, CH, and CP samples can achieve an overpotential of 268, 368, and 373 mV, respectively, to deliver a current density of 10 mA cm^{-2}. In any case, Table 1 summarizes the specific surface area and the electrochemical properties of different catalyst samples. It is surprising that although CPH possesses the smaller SSA compared to CH, CPH still contributes the largest ECSA among all catalyst samples, suggesting that the intrinsic activities of active sites in the CPH catalyst is higher than those of the CP and CH samples.[31] When the specific current density is normalized with respect to ECSA, CPH also exhibits much higher specific current density than CH and CP for the entire voltage range measured (Figure 2e), further confirming that the CPH catalyst is indeed intrinsically more active than CP and CPH. At the same time, a long-term operation test is another important evaluation for eletrocatalysts, which quantify their practicability. To assess the stablilty of the CPH catalyst sample, the water oxidation is performed on the sample at a current density of 10 mA cm^{-2} and then 30 mA cm^{-2} continuously for 75000 s (Figure 2f). It is evident that there is not any significant degradation durng the stablilty measurement. Good stability combined with excellent OER performance demonstrates that CPH can function as an outstanding and robust electrocatalyst. The faradaic efficiency (FE) for overall water splitting was estimated by comparing the volumes of experimentally measured H_2 and O_2 with the theoretically obtained ones (Figure S9). The molar ratio of H_2 and O_2 is close to 2:1, confirming the FE is nearly 100%.

To shed light on the excellent OER performance of CPH, it is essential to first evaluate the precise crystal structure of these nanosheets. Typically, CPH consists of the constituent zigzag double-chained structure, which includes an edge-shared octahedra chain and corner- and edge-shared octahedra connected via phosphate tetrahedra as shown in Figure 3a.[32] It is commonly known that the 6-fold coordination of each Co constituent located within the CoO_6 octahedron would cause severe distortion in the double hexagonal net; therefore, the ladder-like zigzag chain is formed rather than the simple close-packed array (Figure 3b).[32,33] This way, the two phosphate tetrahedra are distorted accordingly in a similar manner (Figure 3c).[32] Previously, it was shown that the hydroxides connected with the zigzag double chain of the phosphate can be beneficial for the rapid M−OOH intermediate formation while this step has been evidenced to be a rate-limiting step for both CP and CH as shown in Tafel plots.[19,34] Also, the irregular circle of the Co atom in the electron density mapping indicates that this unique stacking-disordered phase would induce the electron density imbalance of the constituent species (Figure 3d), which can significantly modulate the electronic structure of the active catalytic site of Co.[24]

In detail, synchrotron radiation X-ray absorption fine structure (XAFS) was then employed to assess further understanding of the electronic structure and the local atomic arrangement of products. Figure 4a shows the absorption edge of the Co K edge spectra of all samples where the peak and threshold position sites in edge-jump region exhibit obvious differences, indicating that Co atoms of these three samples have different local environment and oxidation states.[35] The valence state of Co among these samples can be confirmed

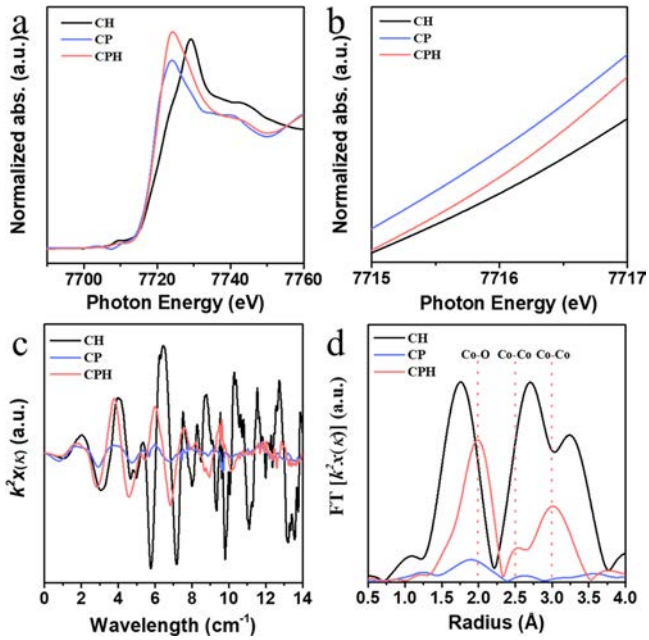

Figure 4. (a) Co K-edge XANES spectra and (b) the magnification of threshold positions in the edge-jump region for an easy view. (c) Corresponding oscillation function $\kappa^2\chi(k)$ for CP, CPH, and CH. (d) Fourier transformation results of CP, CPH, and CH.

following the order of CH > CPH > CP as shown in Figure 4b. Furthermore, the oscillation function of the samples at the wavelength range 0−14 Å show the difference, indicating different main structures (Figure 4c). Extended XAFS was obtained via Fourier transformation (FT) of the XAS curve. As depicted in Figure 4d, there are three main peaks observed for all the samples. The first main peak of CPH located at ∼2 Å is attributed to the single scattering path from the metal ion to the closest crystal oxygen which is consistent with the crystal structure of CPH, confirming the successful preparation of CPH again.[36] At the same time, the existence of other two main peaks of CPH witnessed at 2.5 and 3 Å resulted from the scattering paths from metal ion to closest metal ion, demonstrating the CoO_6 octahedron structure of the CPH catalyst.[36] Also, it is noticed that the peak intensities of Co−O follow the sequence of CH (covalent compound) > CPH > CP (ionic crystal), which suggest the reduced coordination number and the distortion environment around the Co atom in CPH.[37] In this case, the imbalance of electron density in the distorted CoO_6 structure induces the increase of hole states in t_{2g} orbital, beneficial for the direct electron transfer between surface cations and absorbed −OOH intermediates.[24]

After that, we used X-ray photoelectron spectroscopy (XPS) to explore the surface structure of cycled CPH, which could help us evaluate the origin of the observed OER performance and stability. As presented in the deconvoluted Co spectra in Figure 5a, there are two main peaks located at 782.9 and 798.9 eV, which can be assigned to the Co^{2+} bonding for all samples.[2,38] The other two peaks at 780.7 and 796.6 eV can be ascribed to the characteristic peaks of Co^{3+} bonding, while the rest at 786.4 and 803.2 eV are the satellite peaks.[2,38] Obviously, the ratio between Co^{3+}/Co^{2+} increases after reaction because of the oxidation progress under the applied potential. The high-resolution XPS profile of CPH O 1s region can reveal the existence of two different oxygen species before reaction (Figure 5b). The peak located at 531 eV is commonly

DOI: 10.1021/acsami.9b11594
ACS Appl. Mater. Interfaces 2019, 11, 38633−38640

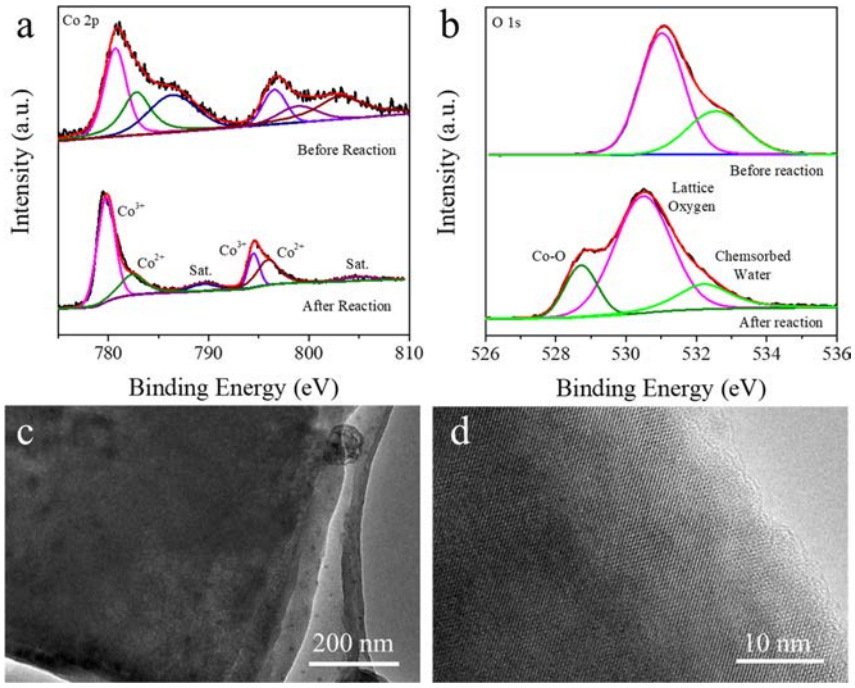

Figure 5. XPS spectra of (a) Co $2p_{3/2}$ region and (b) O 1s region of CPH before and after OER stability test; (c) TEM and (d) HRTEM of CPH after OER stability test.

associated with the oxygen from phosphate groups and hydroxyl groups, while the peak appearing at 532.6 eV refers to the oxygen species in the surface-adsorbed H_2O molecule.[39] After OER stability test, an additional peak at 528.7 appears, which can be assigned to the Co−O bond. Obviously, a large amount of surface hydroxides and oxyhydroxides are formed under anodic potential.[40] It is also noted that a contact angle test is performed with deposition of a droplet (1 M KOH) on different catalyst flakes as shown in the Supporting Information (Figure S10). This droplet is seen to cover the entire surface of CPH and CH samples, whereas a contact angle of 27.2° appears on the surface of CP. This phenomenon is due to the existence of OH in both CPH and CH. More importantly, apart from enhancement of formation of active species, these better wetting characteristics between the CPH surface and the alkaline reactant would further improve the surface contact properties of CPH for enhanced OER performance.[41] Furthermore, the TEM and HRTEM images confirm the clear crystal lattice without the amorphous layer formation on the edge or the severe structure change, indicating the excellent stability and sustainability (Figure 5c,d). Similar to the previous reports of $Ni_{11}(HPO_3)_8(OH)_6$ and Co pyrophosphates, the phosphate of CPH can not only maintain the structure integrity but also improve the structure flexibility, which is consistent with the HRTEM image depicted above.[19,25]

CONCLUSIONS

In summary, two-dimensional cobalt phosphate hydroxides, $Co_5(PO_4)_4OH_2$, a unique class of metal phosphate hydroxide with stacking-disordered phase, are successfully prepared and explored for the first time to serve as high-performance electrocatalysts for water oxidation. Specifically, with use of these catalysts, the small overpotential of 254 mV is witnessed to drive a current density of 10 mA cm^{-2} with a small Tafel slope of 57 mV dec^{-1} for oxygen evolution reaction. A continuous operation for more than 20 h also reveals the robustness and stability of these catalysts in alkaline solutions. After careful analysis, the excellent performance of these hydroxide nanosheets can be attributed to the abundant electrochemical active sites existing in the constituent zigzag edges of distorted CoO_6 octahedron, improvement of active species formation, and their outstanding hydrophilic characteristics. Evidently, this work has opened a new pathway to the rational design of promising metal phosphate hydroxides toward the highly efficient electrochemical energy conversion.

ASSOCIATED CONTENT

Supporting Information

The Supporting Information is available free of charge on the ACS Publications website at DOI: 10.1021/acsami.9b11594.

Physical characterizations and electrochemical data analyses (PDF)

AUTHOR INFORMATION

Corresponding Authors

*E-mail: johnnyho@cityu.edu.hk (J.C.H.).
*E-mail: lin.yg@nsrrc.org.tw (Y.L.).

ORCID

Xiuming Bu: 0000-0002-2372-2271
Renjie Wei: 0000-0002-0459-7196
Yangyang Li: 0000-0003-4153-9558
YanGu Lin: 0000-0002-4210-7709
Johnny C. Ho: 0000-0003-3000-8794

Author Contributions

▲X.B. and C.L.C. contributed equally to this work.

Notes

The authors declare no competing financial interest.

DOI: 10.1021/acsami.9b11594
ACS Appl. Mater. Interfaces 2019, 11, 38633−38640

■ ACKNOWLEDGMENTS

This work is financially supported by the National Natural Science Foundation of China (Grants 51672229), the Science Technology and Innovation Committee of Shenzhen Municipality (Grant JCYJ20170818095520778), the City University of Hong Kong (Project 9610427), and a grant from the Shenzhen Research Institute, City University of Hong Kong.

■ REFERENCES

(1) Seh, Z. W.; Kibsgaard, J.; Dickens, C. F.; Chorkendorff, I.; Nørskov, J. K.; Jaramillo, T. F. Combining Theory and Experiment in Electrocatalysis: Insights into Materials Design. *Science* **2017**, *355*, eaad4998.

(2) Wei, R.; Fang, M.; Dong, G.; Lan, C.; Shu, L.; Zhang, H.; Bu, X.; Ho, J. C. High-Index Faceted Porous Co_3O_4 Nanosheets with Oxygen Vacancies for Highly Efficient Water Oxidation. *ACS Appl. Mater. Interfaces* **2018**, *10*, 7079−7086.

(3) Yan, K.; Lu, Y. Direct Growth of MoS_2 Microspheres on Ni Foam as a Hybrid Nanocomposite Efficient for Oxygen Evolution Reaction. *Small* **2016**, *12*, 2975−2981.

(4) Xu, L.; Zou, Y.; Xiao, Z.; Wang, S. Transforming Co_3O_4 Nanosheets into Porous N-Doped Co_xO_y Nanosheets with Oxygen Vacancies for the Oxygen Evolution Reaction. *J. Energy Chem.* **2019**, *35*, 24−29.

(5) Hao, S.; Chen, L.; Yu, C.; Yang, B.; Li, Z.; Hou, Y.; Lei, L.; Zhang, X. NiCoMo Hydroxide Nanosheet Arrays Synthesized via Chloride Corrosion for Overall Water Splitting. *ACS Energy Lett.* **2019**, *4*, 952−959.

(6) Liu, W.; Liu, H.; Dang, L.; Zhang, H.; Wu, X.; Yang, B.; Li, Z.; Zhang, X.; Lei, L.; Jin, S. Amorphous Cobalt−Iron Hydroxide Nanosheet Electrocatalyst for Efficient Electrochemical and Photo-Electrochemical Oxygen Evolution. *Adv. Funct. Mater.* **2017**, *27*, 1603904−1603914.

(7) Zhou, P.; He, J.; Zou, Y.; Wang, Y.; Xie, C.; Chen, R.; Zang, S.; Wang, S. Single-Crystalline Layered Double Hydroxides with Rich Defects and Hierarchical Structure by Mild Reduction for Enhancing the Oxygen Evolution Reaction. *Sci. China: Chem.* **2019**, DOI: 10.1007/s11426-019-9511-x.

(8) Yu, L.; Xia, B. Y.; Wang, X.; Lou, X. W. General Formation of M-MoS3 (M = Co, Ni) Hollow Structures with Enhanced Electrocatalytic Activity for Hydrogen Evolution. *Adv. Mater.* **2016**, *28*, 92−97.

(9) Tackett, B. M.; Sheng, W.; Chen, J. G. Opportunities and Challenges in Utilizing Metal-Modified Transition Metal Carbides as Low-Cost Electrocatalysts. *Joule* **2017**, *1*, 253−263.

(10) Masa, J.; Sinev, I.; Mistry, H.; Ventosa, E.; de la Mata, M.; Arbiol, J.; Muhler, M.; Roldan Cuenya, B.; Schuhmann, W. Ultrathin High Surface Area Nickel Boride (Ni_xB) Nanosheets as Highly Efficient Electrocatalyst for Oxygen Evolution. *Adv. Energy Mater.* **2017**, *7*, 1700381.

(11) Jin, S. Are Metal Chalcogenides, Nitrides, and Phosphides Oxygen Evolution Catalysts or Bifunctional Catalysts? *ACS Energy Lett.* **2017**, *2*, 1937−1938.

(12) Pei, Z.; Li, H.; Huang, Y.; Xue, Q.; Huang, Y.; Zhu, M.; Wang, Z.; Zhi, C. Texturing in Situ: N,S-Enriched Hierarchically Porous Carbon as a Highly Active Reversible Oxygen Electrocatalyst. *Energy Environ. Sci.* **2017**, *10*, 742−749.

(13) Zhang, Y.; Fan, X.; Jian, J.; Yu, D.; Zhang, Z.; Dai, L. A General Polymer-Assisted Strategy Enables Unexpected Efficient Metal-Free Oxygen-Evolution Catalysis on Pure Carbon Nanotubes. *Energy Environ. Sci.* **2017**, *10*, 2312−2317.

(14) Kanan, M. W.; Nocera, D. G. In Situ Formation of an Water Containing Phosphate and Co^{2+}. *Science* **2008**, *321*, 1072−1075.

(15) Zhan, Y.; Lu, M.; Yang, S.; Liu, Z.; Lee, J. Y. The Origin of Catalytic Activity of Nickel Phosphate for Oxygen Evolution in Alkaline Solution and Its Further Enhancement by Iron Substitution. *ChemElectroChem* **2016**, *3*, 615−621.

(16) Menezes, P. W.; Indra, A.; Das, C.; Walter, C.; Göbel, C.; Gutkin, V.; Schmeißer, D.; Driess, M. Uncovering the Nature of Active Species of Nickel Phosphide Catalysts in High-Performance Electrochemical Overall Water Splitting. *ACS Catal.* **2017**, *7*, 103−109.

(17) Yan, Y.; Xia, B. Y.; Ge, X.; Liu, Z.; Fisher, A.; Wang, X. A Flexible Electrode Based on Iron Phosphide Nanotubes for Overall Water Splitting. *Chem. - Eur. J.* **2015**, *21*, 18062−18067.

(18) Irshad, A.; Munichandraiah, N. High Catalytic Activity of Amorphous Ir-Pi for Oxygen Evolution Reaction. *ACS Appl. Mater. Interfaces* **2015**, *7*, 15765−15776.

(19) Menezes, P. W.; Panda, C.; Loos, S.; Bunschei-Bruns, F.; Walter, C.; Schwarze, M.; Deng, X.; Dau, H.; Driess, M. A Structurally Versatile Nickel Phosphite Acting as a Robust Bifunctional Electrocatalyst for Overall Water Splitting. *Energy Environ. Sci.* **2018**, *11*, 1287−1298.

(20) Yuan, C.-Z.; Jiang, Y.-F.; Wang, Z.; Xie, X.; Yang, Z.-K.; Yousaf, A. B.; Xu, A.-W. Cobalt Phosphate Nanoparticles Decorated with Nitrogen-Doped Carbon Layers as Highly Active and Stable Electrocatalysts for the Oxygen Evolution Reaction. *J. Mater. Chem. A* **2016**, *4*, 8155−8160.

(21) Liu, B.; Peng, H. Q.; Ho, C. N.; Xue, H.; Wu, S.; Ng, T. W.; Lee, C. S.; Zhang, W. Mesoporous Nanosheet Networked Hybrids of Cobalt Oxide and Cobalt Phosphate for Efficient Electrochemical and Photoelectrochemical Oxygen Evolution. *Small* **2017**, *13*, 1701875.

(22) Chen, X.; Li, P.; Jin, Z.; Meng, Y.; Yuan, H.; Xiao, D. Trimetallic phytate in situ electrodeposited on 3D Ni Foam as a Highly Efficient Electrocatalyst for Enhanced Overall Water Splitting. *J. Mater. Chem. A* **2017**, *5*, 18786−18792.

(23) Shao, M.; Chang, Q.; Dodelet, J.-P.; Chenitz, R. Recent Advances in Electrocatalysts for Oxygen Reduction Reaction. *Chem. Rev.* **2016**, *116*, 3594−3657.

(24) Huang, J.; Chen, J.; Yao, T.; He, J.; Jiang, S.; Sun, Z.; Liu, Q.; Cheng, W.; Hu, F.; Jiang, Y.; Pan, Z.; Wei, S. CoOOH Nanosheets with High Mass Activity for Water Oxidation. *Angew. Chem., Int. Ed.* **2015**, *54*, 8722−8727.

(25) Kanan, M. W.; Yano, J.; Surendranath, Y.; Dinca, M.; Yachandra, V. K.; Nocera, D. G. Structure and Valency of a Cobalt-Phosphate Water Oxidation Catalyst Determined by in Situ X-Ray Spectroscopy. *J. Am. Chem. Soc.* **2010**, *132*, 13692−13701.

(26) Wu, A.; Xie, Y.; Ma, H.; Tian, C.; Gu, Y.; Yan, H.; Zhang, X.; Yang, G.; Fu, H. Integrating the Active OER and HER Components as the Heterostructures for the Efficient Overall Water Splitting. *Nano Energy* **2018**, *44*, 353−363.

(27) Tian, J.; Cheng, N.; Liu, Q.; Sun, X.; He, Y.; Asiri, A. M. Self-Supported NiMo Hollow Nanorod Array: An Efficient 3D Bifunctional Catalytic Electrode for Overall Water Splitting. *J. Mater. Chem. A* **2015**, *3*, 20056−20059.

(28) Duan, J.; Chen, S.; Vasileff, A.; Qiao, S. Z. Anion and Cation Modulation in Metal Compounds for Bifunctional Overall Water Splitting. *ACS Nano* **2016**, *10*, 8738−8745.

(29) Wan, J.; Wu, J.; Gao, X.; Li, T.; Hu, Z.; Yu, H.; Huang, L. Structure Confined Porous Mo_2C for Efficient Hydrogen Evolution. *Adv. Funct. Mater.* **2017**, *27*, 1703933.

(30) Kang, B. K.; Woo, M. H.; Lee, J.; Song, Y. H.; Wang, Z.; Guo, Y.; Yamauchi, Y.; Kim, J. H.; Lim, B.; Yoon, D. H. Mesoporous Ni−Fe Oxide Multi-Composite Hollow Nanocages for Efficient Electrocatalytic Water Oxidation Reactions. *J. Mater. Chem. A* **2017**, *5*, 4320−4324.

(31) Zhang, L.; Liu, P. F.; Li, Y. H.; Wang, C. W.; Zu, M. Y.; Fu, H. Q.; Yang, X. H.; Yang, H. G. Accelerating Neutral Hydrogen Evolution with Tungsten Modulated Amorphous Metal Hydroxides. *ACS Catal.* **2018**, *8*, 5200−5205.

(32) Ruszala, F. A.; Anderson, J. B.; Kostiner, E. Crystal Structures of Two Isomorphs of Arsenoclasite: $Co_5(PO_4)_2(OH)_4$ and $Mn_5(PO_4)_2(OH)_4$. *Inorg. Chem.* **1977**, *16*, 2417−2422.

(33) Ghose, S. The Crystal Structure of Hydrozincite, $Zn_5(OH)_6(CO_3)_2$. *Acta Crystallogr.* **1964**, *17*, 1051−1057.

DOI: 10.1021/acsami.9b11594
ACS Appl. Mater. Interfaces 2019, 11, 38633−38640

(34) Wang, X.; Cai, Z.-F.; Wang, D.; Wan, L.-J. Molecular Evidence for the Catalytic Process of Cobalt Porphyrin Catalyzed Oxygen Evolution Reaction in Alkaline Solution. *J. Am. Chem. Soc.* **2019**, *141*, 7665−7669.
(35) Zhang, J.; Xiao, W.; Xi, P.; Xi, S.; Du, Y.; Gao, D.; Ding, J. Activating and Optimizing Activity of CoS_2 for Hydrogen Evolution Reaction through the Synergic Effect of N Dopants and S Vacancies. *ACS Energy Lett.* **2017**, *2*, 1022−1028.
(36) Wang, H. Y.; Hung, S. F.; Chen, H. Y.; Chan, T. S.; Chen, H. M.; Liu, B. In Operando Identification of Geometrical-Site-Dependent Water Oxidation Activity of Spinel Co_3O_4. *J. Am. Chem. Soc.* **2016**, *138*, 36−39.
(37) He, Q.; Wan, Y.; Jiang, H.; Pan, Z.; Wu, C.; Wang, M.; Wu, X.; Ye, B.; Ajayan, P. M.; Song, L. Nickel Vacancies Boost Reconstruction in Nickel Hydroxide Electrocatalyst. *ACS Energy Lett.* **2018**, *3*, 1373−1380.
(38) Yan, Y.; Li, K.; Chen, X.; Yang, Y.; Lee, J.-M. Heterojunction-Assisted Co_3S_4@Co_3O_4 Core-Shell Octahedrons for Supercapacitors and Both Oxygen and Carbon Dioxide Reduction Reactions. *Small* **2017**, *13*, 1701724−1701731.
(39) Feng, J. X.; Ding, L. X.; Ye, S. H.; He, X. J.; Xu, H.; Tong, Y. X.; Li, G. R. $Co(OH)_2$@PANI Hybrid Nanosheets with 3D Networks as High-Performance Electrocatalysts for Hydrogen Evolution Reaction. *Adv. Mater.* **2015**, *27*, 7051−7057.
(40) Indra, A.; Tallarida, M.; Schmeißer, D.; Menezes, P. W.; Strasser, P.; Driess, M.; Das, C.; Bergmann, A.; Sahraie, N. R. Unification of Catalytic Water Oxidation and Oxygen Reduction Reactions: Amorphous Beat Crystalline Cobalt Iron Oxides. *J. Am. Chem. Soc.* **2014**, *136*, 17530−17536.
(41) Han, N.; Yang, K. R.; Lu, Z.; Li, Y.; Xu, W.; Gao, T.; Cai, Z.; Zhang, Y.; Batista, V. S.; Liu, W.; Sun, X. Nitrogen-Doped Tungsten Carbide Nanoarray as an Efficient Bifunctional Electrocatalyst for Water Splitting in Acid. *Nat. Commun.* **2018**, *9*, 924.

DOI: 10.1021/acsami.9b11594
ACS Appl. Mater. Interfaces 2019, 11, 38633−38640